International Journal on Advanced Science Engineering Information Technology

Vol.12 (2022) No. 3
ISSN: 2088-5334

# Combining Pan-Sharpening and Forest Cover Density Transformation Methods for Vegetation Mapping using Landsat-8 Satellite Imagery

Projo Danoedoro [a,*], Diwyacitta Dirda Gupita [b]

[a] *Department of Geographical Information Science, Universitas Gadjah Mada, Bulaksumur, Yogyakarta, 5528, Indonesia*
[b] *Remote Sensing Laboratory, Universitas Gadjah Mada, Bulaksumur, Yogyakarta, 5528, Indonesia*
*Corresponding author: *projo.danoedoro@geo.ugm.ac.id*

***Abstract*— Forest cover density (FCD) transformation is an 8-bit Landsat imagery-based method for vegetation mapping, which uses a set of indices comprising vegetation, soil, shadow, and thermal components. With the advent of 16-bit Landsat-8 imagery, radiometric correction and pan-sharpening methods could be applied to generate new datasets with different spectral and spatial characteristics. This study combined several methods of pan-sharpening and FCD transformations for mapping vegetation density in Salatiga and Ambarawa region, Indonesia, based on Landsat-8 dataset. The imagery was treated differently to constitute five new datasets, *i.e.,* original multispectral imagery (30 m), radiometrically corrected multispectral imagery (30 m), and three pan-sharpening datasets generated using Gram-Schmidt (GS), Principal Component Analysis (PCA), and Hyper-spherical Color Space (HCS) methods (15 m). Each dataset was then processed using FCD transformation as a basis for vegetation density and structural composition mapping. Field observation and vegetation density measurement using high-spatial-resolution imagery was used as a reference for accuracy assessment. This study found that the pan-sharpening methods produced new datasets with various correlation coefficients with their corresponding original bands, affecting the accuracy of spectral modeling in FCD. Moreover, the generated FCD models were found less accurate as compared to that of the original one. However, the accuracy could be increased by rescaling the original DNs and regrouping the original classes into simpler categorization. Besides the problem of data characteristics, all FCD models were also found inaccurate compared to previous studies due to the landscape complexity of the study area.***

***Keywords*— Image processing; radiometric correction; pan-sharpening; vegetation mapping; forest cover density.**

*Manuscript received 13 Jul. 2020; revised 18 Feb. 2021; accepted 30 Apr. 2021. Date of publication 30 Jun. 2022.*


## I. INTRODUCTION

Vegetation mapping based on remotely sensed digital imagery has been a common practice and has become one of the most efficient methods compared to full fieldwork [1]. As viewed from a land-cover/land-use perspective, vegetation mapping usually relies on multispectral classification [2], although sometimes it is combined with vegetation index [3]. In the context of species composition, these activities usually utilize multispectral classification [4], [5], hyperspectral analysis [6]–[8], and a landscape-ecological approach that combines remote sensing and GIS [9]. On the other hand, when the distribution of vegetation density is a measurement target, this activity usually utilizes spectral transformations, especially vegetation indices [10]–[12]. In contrast, it often uses forest cover density or FCD transformation [13] and also visual interpretation [14].

Among various methods that were often used, the utilization of vegetation index, *e.g.,* normalized difference vegetation index (NDVI) was the simplest way and was often more effective [12]. However, departing from a critical view of the lack of various vegetation indices and the need for mapping in the context of the forestry industry, the International Timber Trade Organization (ITTO) developed forest cover density (FCD) transformation to map the density and structural composition of vegetation [13]. Many studies reported that the FCD methods accurately mapped the forest density [15]–[20].

FCD was developed based on Landsat-4 and Landsat-7 datasets which were recorded using 8-bit-coding sensor systems. The developed formulas in the FCD model departed from the assumption that the data has a digital number (DN) range of 0–255 or within an 8-bit coding. In addition, a detailed technical explanation for the pre-processing method has not been given explicitly. On the contrary, the current development shows the availability of data with a 16-bit

coding system (0–65,535) such as Landsat-8 OLI and Sentinel 2, which have blue up to middle infrared bands.

Landsat 8 OLI still has thermal infrared bands like its predecessors, *i.e.*, Landsat-5 TM and Landsat-7 ETM$^{+}$. Besides, the sensor also has a panchromatic band, which allows the product to be combined with other bands in the form of a pan-sharpened dataset. Pan-sharpening itself can be built using several methods such as Brovey, Hue-Saturation-Value (HSV), Gram-Schmidt (GS), Principle Component Analysis (PCA) [21], [22], and Hyperspherical Color Space (HCS) [23]. Brovey and HSV, according to many studies, were found less able to present spectral information under the original multispectral bands [24]–[26].

Nowadays, the radiometric correction methods had developed far more advanced than when the FCD transformation method was initiated. However, the use of the spectral index-based models strongly requires radiometric correction in advance [12], [27]. At present, there are several established methods of radiometric correction such as Dark Object Subtraction (DOS), Cos (Θ), MODTRAN, FLAASH, and full atmospheric correction models [23], [28], which consider many variables. Since the FCD model also works on a spectral basis, a radiometric correction stage should be strongly recommended prior to the derivation of indices within the model.

### A. Problem Formulation

The research problems were formulated as follows.

- The effect of image radiometric correction has never been compared to the original image (without correction) when it was utilized in FCD transformation.
- Pan-sharpening methods can increase spatial resolution and at the same time maintain colors, but there was a lack of knowledge of pan-sharpening methods that are suitable for FCD transformation, concerning their accuracies in vegetation structural composition mapping.

### B. Research Objectives

Based on the previously mentioned problem formulation, three research objectives were specified as follows:

- To undertake radiometric correction of Landsat-8 OLI dataset using full atmospheric correction model as a basis for pan-sharpening and FCD model development.
- To build pan-sharpened images based on a combination of multispectral and panchromatic bands that have been radiometrically corrected, using different pan-sharpening methods, namely GS, PCA, and HCS, and evaluate their quality as compared to the original multispectral bands,
- to build FCD maps based on radiometrically corrected pan-sharpened GS, PCA, and HCS images and to test the accuracy of the resultant vegetation density models with respect to the independent measurement dataset.

### C. Study Area

The study area is located in Salatiga- Ambarawa and its surrounding, Central Java, Indonesia. As shown in Fig. 1, this study area consists of several major landscape units, although volcanic-origin landforms mostly dominate them. A relatively large natural lake called Rawa Pening is located in the middle of the scene, surrounded by an alluvial plain, old volcanoes, and denudational hills with sedimentary rocks.

In terms of vegetation structural composition, the denudational hills are covered with coffee, cocoa, rubber plantations, and a mixed garden. In contrast, the structural hills with limestone and other marine sedimentary rocks are utilized for teak forest and dryland cultivation. Dense forests occupy the upper part of volcanic slopes and cones. Some parts of the forest had been burned, particularly in the south-facing slopes and cones.

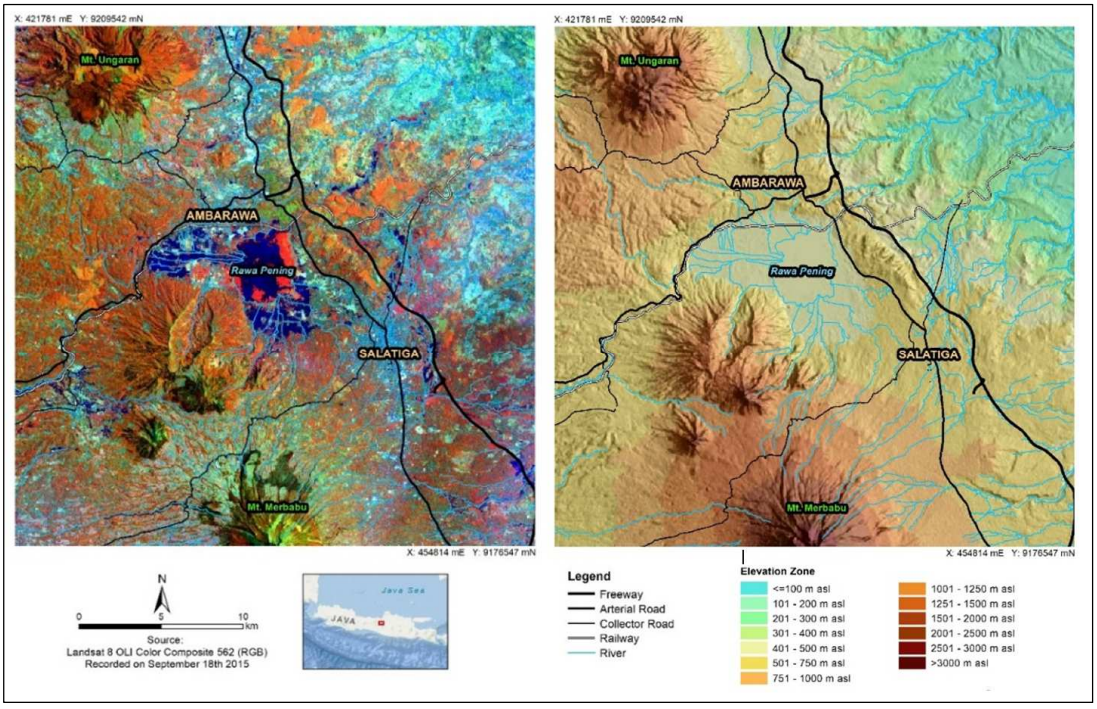


Fig. 1 Landscape arrangement di in the study area, as viewed from vegetation ecological perspective

The elevation of the study area ranges from less than 100m up to 3142m above sea level (asl), making the complexity of the landscape increase due to the distribution of land surface temperature –in addition to the existence of Rawa Pening swampy lake. All these diverse ecological factors constitute a suitable environment for testing the capability of FCD transformation in vegetation mapping.

The elevations zones between 100 – 400 m asl are related to structural hills, mostly with limestone and other marine sedimentary rocks. These areas are mainly occupied for teak plantation forest (deciduous), dry field, rural settlement, and mixed garden. Elevation zones between 401 – 750 m asl are found in the denudational hills with volcanic remnants and marine sedimentary rocks in the north and eastern part and are also found in the volcanic foot slopes. These areas are mainly occupied for rubber, coffee, cocoa plantations, mixed garden, rural/urban settlement (including Salatiga and Ambarawa), and industrial activities. An alluvial plain in this elevation zone containing Rawa Pening swampy lake is covered with an invasive aquatic weed called *enceng gondok* (*Eichhornia crassipes*).

At the higher elevation, mixed forest, pine forest, dry field with vegetables, rural settlement, and tea plantation are commonly found. Particularly at the 2501 m asl or more, grassland, shrubs, bare soil, and burned vegetation are more dominant.

## II. Materials and Methods

### A. Materials

This study made use of Landsat 8 OLI imagery covering Salatiga - Ambarawa and its surrounding, with path/row 120/065, recorded on September 18th 2015, which have been geometrically corrected at T level. This dataset comprises spectral bands of blue (0.450-0.515µm), green (0.525-0.600 µm), red (0.630-0.680 µm), near-infrared (NIR) (0.845-0.885 µm), shortwave infrared I or SWIR1 (1.550-1.660 µm), which are at 30 m spatial resolution, thermal infrared I (10.30-11.30 µm) at 100 m spatial resolution, and panchromatic band at 15 m spatial resolution. In addition to the image above dataset, this study also used WorldView 3 imagery and RBI topographic map at 1:25,000 scale as the basis for field orientation, measurement, and accuracy assessment.

Image processing software for this study were ILWIS 3.8 Open and Idrisi Terrset academic version. Most of the processes, particularly the FCD modeling, were run using map calculator and script programming instead of using menu-based facilities. We intentionally did not use the FCD Mapper software based on the assumption that this study tried to explore the operability of the FCD concepts using any available software concerning the theory and formulas given in previous works [12].

### B. Methods

The research applied four main types of image processing, *i.e.* (a) data preparation comprising radiometric correction and calibration, (b) image pan-sharpening, (c) modeling with the FCD method, and (d) linear transformation of the FCD results as a basis for mapping the vegetation density and structural composition. The final results in the form of vegetation density models were tested according to their accuracy using samples taken from field reference and high-spatial-resolution imagery.

It should be emphasized here that after the first and second processing stages previously mentioned, this study explored five kinds of datasets. The first is the Landsat 8 OLI image (30 m) which was only calibrated to 8-bit dataset as a control. The second is Landsat-8 OLI imagery (30 m) corrected radiometrically with full atmospheric correction. The third until the fifth are pan-sharpened datasets based on full atmospheric correction images that raised to 15 m spatial resolution using three different pan-sharpening methods. Comparing the quality of the corrected and pan-sharpened images was undertaken by analyzing the correlation between their spectral values wand

The research method is summarized in Fig. 2, while each stage of processing is explained as follows:

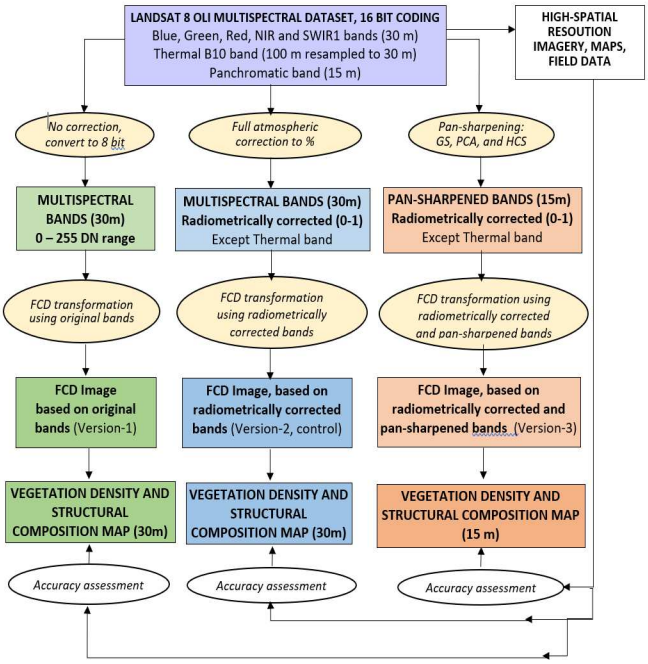


Fig. 2 Research Methods developed in this study

*1) Preparation/Radiometric Correction:* The original Landsat-8 OLI image was available in 16-bit coding format or has a range of digital number (DN) 0 – 65,535. Because the FCD model was developed based on Landsat-5 TM and Landsat-7 ETM+ images which were only recorded in 8-bit range (0 - 255), bit level compression was required from 16- to 8-bits. However, this direct conversion to 8-bits was only applied to the control dataset, while other datasets were treated differently, started from full atmospheric correction only (at 30 m spatial resolution), and radiometric correction followed by pan-sharpening process to 15 m spatial resolution. The radiometric correction transformed image DNs (0 - 65535) to the level of at-surface reflectance (in percent), which used a full atmospheric correction method [23]. The equation of full atmospheric correction was based on the work of [28]:

$$\rho = \frac{(\Pi * (L_\lambda - L_{haze}))}{(\tau_v * (E_o * Cos(T_Z) * \tau_z + E_{down})} \quad (1)$$

where $\rho$ is at-surface reflectance in percent, $L_\lambda$ is the image spectral radiance. $L_{haze}$ is scattered spectral radiance recorded

as the minimum one by the sensor. $\tau_v$ is the atmospheric transmittance or optical thickness of the atmosphere. $E_o$ is the solar spectral irradiance that takes into account the Earth-Sun distance in specific Julian days. $T_z$ is the incident angle of the direct solar flux to the Earth's surface. $E_{down}$ is downwelling spectral irradiance due to the scattered solar flux in the atmosphere.

Practically, this correction took into account image metadata containing information as follows:

- The range of the original DN values or the level of bit-coding.
- Maximum and minimum spectral radiance in Watts $m^{-2}sr^{-1}\mu m^{-1}$ that can be detected by the sensor.
- Sun elevation and azimuth.
- Recording time (date, month and hour) follows the UTC standard.
- Optical thickness of the atmosphere at the time of recording.
- DNs for objects in the form of very dark shadows or very clear and deep water.

*2) Pan-sharpening*: Pan-sharpening in this study covered three methods, namely PCA pan-sharpening (PCA) [21], Gram-Schmidt (GS) [21], [29], and Hyperspherical Color Space (HCS) [23]. In the pan-sharpening PCA method, the multispectral bands of Landsat 8 image were processed by PCA first at 15 m pixel size. From this PCA, PC-1 was evaluated according to its variance and minimum-maximum values, to be replaced by the panchromatic band. Then the pan-sharpening process reversed the dataset containing the panchromatic band, which has replaced the PC-1 position.

GS pan-sharpening involved four steps. First, simulation of the high-resolution panchromatic band based on multispectral bands with lower spatial resolution. Second, the Gram-Schmidt transformation was applied to the simulated panchromatic band and the multispectral band, where the simulated panchromatic band was treated as the first band. Third, the original high-resolution panchromatic band was then replaced by a simulated Gram-Schmidt band. Fourth, the Gram-Schmidt transformation was then reversed.

In the HCS method, the first step was to resample the multispectral bands to the same spatial resolution as that of the panchromatic band, *i.e.,* 15 m. Then, a filter at 7x7 size was used to smooth the panchromatic band and reduce spatial artifacts. Next, the algorithm performed a forward transformation to calculate the intensity and angle according to the original multispectral bands. After that, it calculated the adjusted intensity with the smoothed panchromatic band and resampled multispectral bands. Then, with the mean and standard deviation of transformed multispectral bands, the bands were resampled to match the resolution of the panchromatic band. Lastly, it replaced the intensity and performed a reverse transformation.

*3) Forest Cover Density Modelling (FCD)*: The FCD transformation is a relatively complicated step to reduce the map of vegetation density related to its structural composition if compared with other spectral indices such as vegetation index and soil moisture indices [30], [31], [32], [33]. FCD includes three main steps [12], namely (a) preparation of basic indices, *i.e.,* Advanced Vegetation Index or AVI, Bare Soil Index or BI, Shadow Index or SI and Thermal Index or TI; (b) the preparation of a derivative index, *i.e.,* Vegetation Density or VD as the result of the integration of AVI with BI; and Shadow Scaled Index or SSI as a combination of SI and TI; (c) FCD itself which is an integration of VD with SSI.

AVI involved the red (Red) and near-infrared (NIR) bands. Since this formula contains NIR-Red terms, it is possible that the results obtained from NIR-Red <0, so that the following conditions were required:

IF (NIR-Red) ≤ 0,
THEN AVI= 0,

$$\text{ELSE } AVI = \sqrt[3]{(NIR+1)*(256-Red)*(NIR-Red)} \quad (2)$$

BI was obtained by involving the first shortwave infrared (SWIR1), near-infrared (NIR), red (Red), and Blue (Blue) bands with the following formula:

$$BI = \left(\left(\frac{(SWIR1+Red)-(NIR+Blue)}{WIR1+Red)+(NIR+Blue)}\right)*100\right)+100 \quad (3)$$

Where is $0 \leq BI \leq 200$

These AVI and BI images were then integrated using PCA, where the first principal component (PC-1) was taken as the VD or vegetation density image. These results were then transformed linearly into a new image with the 0 -100 range, where 0 indicated bare soil (0% vegetation cover) and 100 indicated forest with 100% vegetation cover.

SI image was generated by involving blue, green, and red bands, with the following formula:

$$SI = \sqrt[3]{(256-Blue)*(256-Green)*(256-Red)} \quad (4)$$

The thermal channel image was converted to a spectral radiance image $L_{\lambda\_image}$ through the following formula:

$$L_{\lambda\_image} = L_{\lambda\_min} + \left(\frac{L_{\lambda\_max}-L_{\lambda\_min}}{DN_{max}} * DN_{image}\right) \quad (5)$$

Where $L_{\lambda_min}$is the minimum detectable spectral radiance value in the corrected band, $L_{\lambda_max}$is the maximum detectable spectral radiance value, $DN_{max}$ is the maximum DN of the original image (in 16-bit coding means 65,535), while $DN_{image}$ denotes all image's DNs to be calibrated to spectral radiance in Watt $m^{-2}sr^{-1}\mu m^{-1}$. The value $L_{\lambda\_min}$ This new image was then converted to 8-bit system (0-255) and used as the thermal index image (TI).

In the next step, the SI and the TI images were then integrated with the PCA method to derive a new image called the Scaled Shadow Index (SSI). Areas with SSI value = 0 were regions with shadow value (SI) = 0 too. The area where SSI = 100 was the area with 100% shadow cover. This value range was then used as a basis for scaling back the SI value into a normalized SSI through a linear transformation process, where the original SI range was changed to 0-100, to represent the percentage of 0-100% vegetation cover.

Finally, the FCD map was derived from the VD and SSI images using the following formula:

$$FCD = \left(\sqrt{(VD*SSI)+1}\right)-1 \quad (6)$$

where it was assumed that FCD would have a range of 0 - 100, with 0 representing open land and 100 representing very dense vegetation with multiple layers (multi-story). In this

study, the FCD pixel values were then required reclassification [18], [34] as shown in Table I.

*4). Accuracy Assessment:* Accuracy assessment was based on the field observation and vegetation density measurement using high-spatial-resolution imagery. The accuracy assessment was carried out using two methods, *i.e.,* standard error of estimates (SE)-based accuracy for the original ratio data containing a percentage of vegetation density and confusion matrix for vegetation structural composition categories. A total of 112 samples were selected using stratified random sampling as a basis for accuracy assessment and were evenly distributed concerning the spatial distribution of the FCD classes in the study area.

## III. Results and Discussion

### A. Radiometric Correction Results

Radiometric calibration and correction were applied to the spectral bands involved in FCD modeling, namely blue, green, red, NIR, SWIR1, and thermal infrared. For blue up to SWIR1 bands, the correction process was carried out up to at-surface reflectance (in %), while the thermal infrared DNs were only calibrated to spectral radiance values in Watt $m^{-2}sr^{-1}\mu m^{-1}$, according to the standard in FCD modeling. The full atmospheric correction converted DNs to the percentage of reflectance, which means that the original range of 16-bit, *i.e.*, 0 – 65,535 were transformed to 0-1.

TABLE I
FCD classification of final pixel values concerning vegetation density, and structural composition

| Cls | Value Range | Vegetation structural composition description |
|---|---|---|
| 0 | 0 | Bare soil |
| 1 | 1-10 | No canopy coverage. Open land and grass are predominant |
| 2 | 11-20 | Tree canopies began to emerge but open land is still predominant, |
| 3 | 21-30 | Tree canopies occupy 11-20% of the pixel area but open land is still predominant |
| 4 | 31-40 | Tree canopies occupy 21-30% of the pixel area interleaved with bushes and shrubs |
| 5 | 41-50 | Young tree canopies develop and cover 41-50% of the pixel area, with a predominance of shrubs while shrubs decrease. |
| 6 | 51-60 | Adult and young tree canopies are growing, covering 51-60% of the pixel area, which is starting to show a difference |
| 7 | 61-70 | Tree canopies are growing rapidly, covering 61-70% of the pixel area with differences in strata of stands, clearly visible and heterogeneous |
| 8 | 71-80 | Tree canopies cover 71-80% of the pixel area with distinct strata standing distinctions; species heterogeneity is increasing, |
| 9 | 81-90 | Tree canopies cover 81-90% of the pixel area with different standing strata; very clearly seen, very high heterogeneity |
| 10 | 91-100 | Tree canopies cover 91-100% of the pixel area with very stratified differences, very high heterogeneity, sunlight is unable to reach the forest floor, and moisture is very high. |

In the radiometric correction results, we found several pixels with values exceeding 1.00. However, this anomaly was only presented by few pixels, *i.e.*, less than 0.001% of the total. In addition, the anomalous values also only appeared in the NIR and SWIR1 bands due to the difficulty in determining the exact measures of optical thickness for longer wavelengths and the problem in specifying sky diffuse irradiance values during the modeling. The diffuse sky irradiance was set to 0 if there is no available data [22]. The same radiometric correction as in the blue up to SWIR1 bands was also applied to the panchromatic band.

### B. Pan-sharpening Results

The pan-sharpening process delivered three types of pan-sharpened datasets, corresponding to the methods used, *i.e.*, GS, PCA, and HCS. All pan-sharpened bands have the same spatial resolution. *i.e.,* 15 m. However, in terms of spectral information contents, they performed slight differences that could be visually and statistically analyzed. Fig. 3 shows an example of a pan-sharpened color composite image (NIR-SWIR1-Blue, for R-G-B color composition), which was processed using the HCS method.

The pan-sharpened images did not exhibit a significant improvement in spectral and spatial details due to the slight difference in the spatial resolution of image inputs compared to pans-sharpening of ALOS imagery, for example, in [26]. The Landsat-8 multispectral bands are 30 m, while and the panchromatic band is only 15 m. However, this difference could still provide different operational mapping scales, *i.e.*, 1:100,000 and 1:50,000 respectively [5], [35]

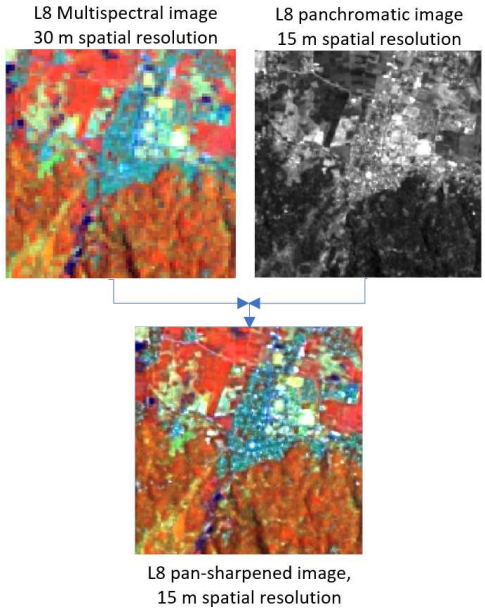


Fig. 3 An example of pan-sharpening result using HCS method, covering small part of the study area.

Statistically, the spectral information contents of the pan-sharpened datasets were also different. This study used the radiometrically corrected dataset as a reference so that the other image datasets, including the original bands without correction, were also compared. As shown in Table II, two datasets with 30 m spatial resolution had been correlated. We found that the between-band correlations were very high for the same wavelength regions (bold font), *i.e.*, 0.965. In this context, high correlation means that a pair is similar. Therefore it could be expected that the original bands without

correction might give similar results in the spectral-based image modeling.

This study also found different results from three pan-sharpened image datasets, as shown in Tables III-V as examples for GS, PCA, and HCS pan-sharpened images. The GS pan-sharpening method generated a relatively lower average correlation between corresponding bands than PCA and HCS methods. The average $r_{GS}$ was 0.891, while the average $r_{PCA}$ and $r_{HCS}$ were 0.907 and 0.897, respectively. However, the difference between those correlation coefficients were also relatively small.

TABLE II
CORRELATION MATRIX BETWEEN RADIOMETRICALLY CORRECTED BANDS AND THE ORIGINAL BANDS (WITHOUT CORRECTION).

| | | Original bands, no correction | | | | |
|---|---|---|---|---|---|---|
| | | **Blue** | **Green** | **Red** | **NIR** | **SW1** |
| **Radiometrically corrected bands** | **Blue** | **0.910** | 0.887 | 0.847 | -0.038 | 0.687 |
| | **Green** | 0.918 | **0.948** | 0.912 | 0.027 | 0.763 |
| | **Red** | 0.928 | 0.960 | **0.980** | -0.108 | 0.808 |
| | **NIR** | -0.127 | -0.028 | -0.141 | **0.994** | 0.258 |
| | **SWIR1** | 0.718 | 0.782 | 0.799 | 0.264 | **0.994** |

TABLE III
CORRELATION MATRIX BETWEEN RADIOMETRICALLY CORRECTED BANDS AND THE PAN-SHARPENED BANDS (GS METHOD)

| | | Pan-sharpened bands (GS method) | | | | |
|---|---|---|---|---|---|---|
| | | **P+Blue** | **P+Green** | **P+Red** | **P+NIR** | **P+SW1** |
| **Radiometrically corrected bands** | **Blue** | **0.901** | 0.852 | 0.841 | -0.397 | 0.473 |
| | **Green** | 0.889 | **0.887** | 0.878 | -0.335 | 0.520 |
| | **Red** | 0.857 | 0.857 | **0.893** | -0.418 | 0.538 |
| | **NIR** | -0.143 | -0.046 | -0.159 | **0.950** | 0.197 |
| | **SW1** | 0.821 | 0.849 | 0.891 | -0.131 | **0.826** |

TABLE IV
CORRELATION MATRIX BETWEEN RADIOMETRICALLY CORRECTED BANDS AND THE PAN-SHARPENED BANDS (PCA METHOD)

| | | Pan-sharpened bands (PCA method) | | | | |
|---|---|---|---|---|---|---|
| | | **P+Blue** | **P+Green** | **P+Red** | **P+NIR** | **P+SW1** |
| **Radiometrically corrected bands** | **Blue** | **0.910** | 0.871 | 0.833 | -0.251 | 0.487 |
| | **Green** | 0.890 | **0.902** | 0.865 | -0.168 | 0.538 |
| | **Red** | 0.874 | 0.888 | **0.898** | -0.269 | 0.561 |
| | **NIR** | -0.154 | -0.057 | -0.165 | **0.959** | 0.219 |
| | **SW1** | 0.809 | 0.859 | 0.866 | 0.100 | **0.865** |

TABLE V
CORRELATION MATRIX BETWEEN RADIOMETRICALLY CORRECTED BANDS AND THE PAN-SHARPENED BANDS (HCS METHOD)

| | | Pan-sharpened bands (HCS method) | | | | |
|---|---|---|---|---|---|---|
| | | **P+Blue** | **P+Green** | **P+Red** | **P+NIR** | **P+SW1** |
| **Radiometrically corrected bands** | **Blue** | **0.910** | 0.888 | 0.858 | -0.121 | 0.658 |
| | **Green** | 0.883 | **0.907** | 0.880 | -0.038 | 0.708 |
| | **Red** | 0.886 | 0.913 | **0.931** | -0.133 | 0.752 |
| | **NIR** | -0.036 | 0.061 | -0.034 | **0.847** | 0.297 |
| | **SW1** | 0.682 | 0.739 | 0.755 | 0.200 | **0.890** |

The quality of pan-sharpened images also depends on the bandwidth and the bandwidth overlap of the high-spatial-resolution image [20]. The bandwidth of the panchromatic band of Landsat 8 is 0.503 - 0676 µm, while the NIR and SWIR-1 bands are beyond this range. Therefore, only visible bands could provide higher correlation coefficients as compared to the infrared bands.

The contributors to the low correlation coefficients in each dataset were also different. In GS and PCA methods, the low $r_{GS}$ were mainly contributed by the SWIR1+P pair, while in HCS, the NIR+P band played a more important role. These results were understandable since it has been mentioned that PCA and GS used similar approaches to the methods, where inverse PCA techniques were used and modified [20].

### *C. Forest Cover Density Modelling*

Based on the FCD modeling, five maps of forest cover density have been produced. The first map came from the original bands without correction (30 m), the second one was based on the radiometrically corrected bands (30 m), and the last three were vegetation density maps derived using GS, PCA, and HCS pan-sharpened bands, respectively.

*1) FCD Model based on Original Dataset*: Using the original dataset without correction, all involved bands were only compressed into 8-bit images (DN range= 0-255) since the beginning of processing. This study put all required bands in the equations (2), (3), and (4). The AVI, BI, and SI images were also kept in the DN range of 0-255. However, when the PCA process was run to integrate AVI and BI images as well as SI and TI images, the resultant indices (VD dan SSI) required to be rescaled into 8-bit image, with 0-100 range. The FCD map generated from equation (6) is presented in Fig 4a-1.

*2) FCD Model based on Full Atmospheric Correction:* All atmospherically corrected bands were converted to 8-bit images in this modeling. Prior to the conversion, the thermal band was transformed into spectral radiance first using equation (5). After that, they were input to the equations (2), (3), and (4) in order to derive AVI, BI and SI images. All those images were rescaled to 8-bit images as well. Similar principal component analysis and processing were applied to the derived data plus thermal image for generating VI and SSI, which were then rescaled to 0-100. As a result, a FCD model is presented in Fig 4b-1.

*3) FCD based on Pan-sharpened Datasets:* Three different pan-sharpened datasets, *i.e.,* using GS, PCA, and HCS methods, respectively, were used to input the FCD modeling. The same procedure was described in the use of full atmospherically corrected bands applied. The difference was only in the spatial resolution of these three datasets, which is 15 m, compared to 30 m of the original bands. However, this study needed to resample the thermal band into 15 m pixel size since FCD modeling only works when all input bands have the same pixel size. The resampling process used nearest-neighbor interpolation in order to retain the original pixel values [20]. Resultant FCD models are presented in Figs 4c-1, 4d-1 and 4e-1 respectively.

Figs. 4a-1 up to 4e-1 show that every dataset produced different vegetation density values. The minima and maxima

contained by the images also show that no one has a significant number of pixels with 0 value or bare soil. However, it was impossible because the study area has relatively large patches of bare soil, freeway/toll road construction, urban building, and even water body with no vegetation. All those land-cover types looked yellowish-green, which means that they were identified as vegetated areas. Based on the statistical analysis of each derived FCD, the minima were above 30 or --according to Table II—were identified as bushland interleaved by trees.

These findings did not meet with the concept of FCD mapping proposed by Dewa and Danoedoro [12], which was confirmed by some other studies [2], [36], [37][38]. The final processing of FCD was performed by applying equation (6). However, other studies using FCD also undertook additional processes, including regression analysis with field data [39]–[41], or in combination with other methods such as vegetation index [42].

Based on the immediate results using equation (6), this study tried to rescale the FCD images by considering the minima and maxima correlated with the minima and maxima of vegetation density found in the field. Therefore, the resultant FCD images were rescaled using those reference values. This method was more practical than trying to develop a regression-based equation using many samples of field measurement. Besides, the regression-based equation is more similar to the use of vegetation index-based mapping [43], [44], while FCD transformation was originally developed for the direct assessment using density slicing of the immediate result of FCD [13]. The rescaled original FCD image values generated new FCD maps, as shown in Figs. 4a-2 up to 4e-2 respectively. The new pixel value ranges were then classified concerning the 11 categories of vegetation density and structural composition described by [13] and [18] in Table I.

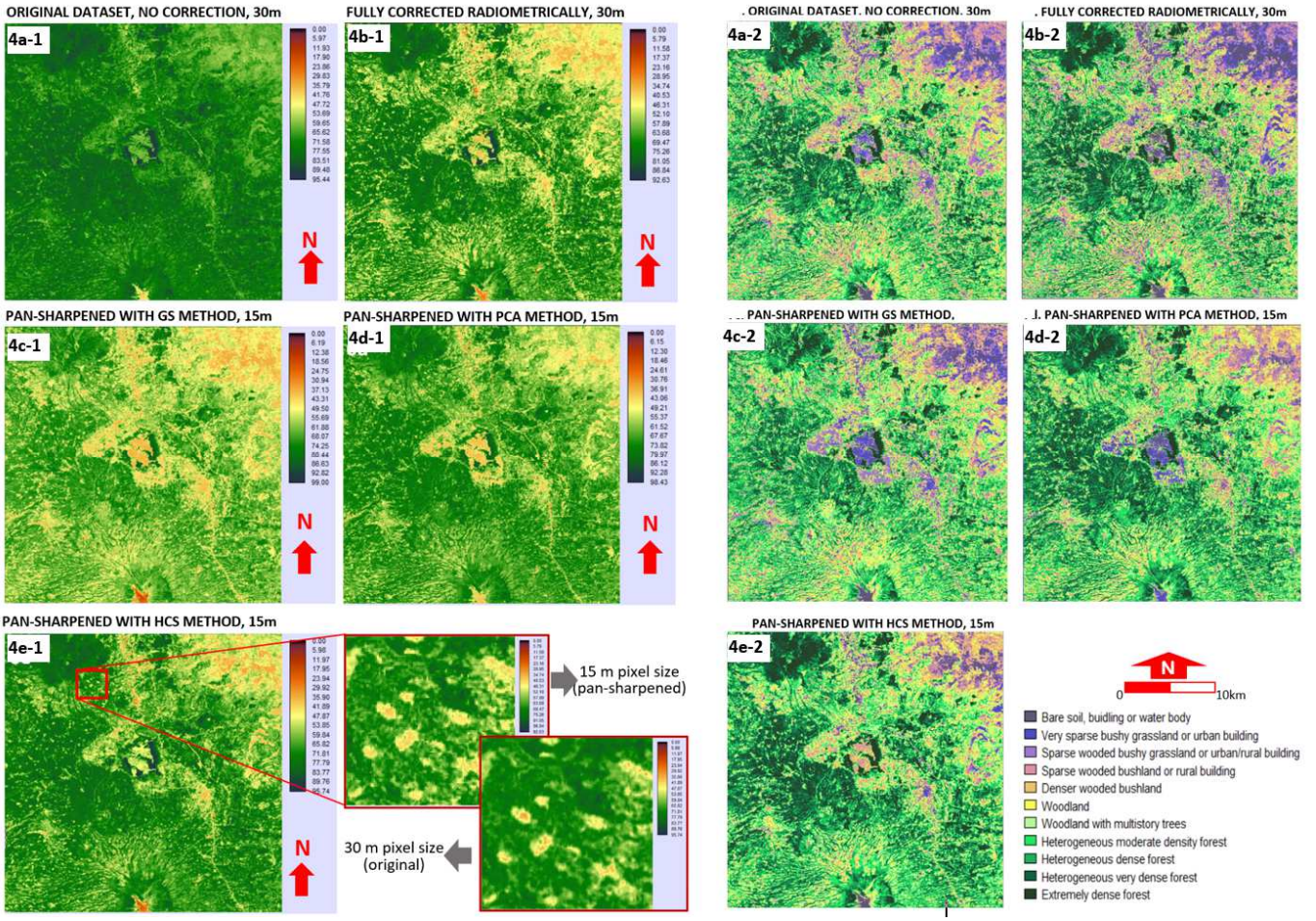


Fig. 4 FCD images that were generated using 30 m Landsat 8 multispectral dataset (4a-1 and 4b-1) and were derived using Landsat 8 pan-sharpened dataset (4c-1, 4d-1 and 4e-1). Each legend is separated from others due to different ranges. Figs 4a-2 up to 4e-2 depict FCD maps based on rescaled FCD images by correlating minimum and maximum values with the minimum and maximum vegetation density found in the field.

To obtain more precise comparison, a correlation analysis among corresponding bands were carried out. All original datasets were then resampled to 15 m pixel size first. Correlation analysis between FCD models as the immediate results of equation (6) showed that the pan-sharpened image-based FCDs had lower correlation coefficients with the original bands-based FCD as well as with the radiometrically corrected original bands-based FCD. This finding was consistent with the correlation matrix between corresponding bands presented in Tables II – V. Table VI shows this result.

After the rescaling, there was no significant change in the correlation between the original bands and the ones that have been pan-sharpened, as shown in Table VII. It is interesting to see that FCD model generated using both GS and PCA pan-

sharpened images took advantage of the rescaling process to increase the correlation coefficients. However, it was not the case with the FCD model derived using HCS pan-sharpened images, which slightly decreased in correlation coefficient with the standard, radiometrically corrected image. This is related to the FCD histogram, where HCS-based FCD shows more distributed values across the range.

TABLE VI
CORRELATION MATRIX BETWEEN ORIGINAL, FULL-RADIOMETRICALLY CORRECTED, AND PAN-SHARPENED -BASED FCD IMAGES (BEFORE RESCALING)

| | FCD Image based on the Input Data | | | | |
|---|---|---|---|---|---|
| | **Original** | **Rad_Corr** | **GS** | **PCA** | **HCS** |
| **Original** | **1.00** | 0.97 | 0.92 | 0.91 | 0.93 |
| **Rad_Corr** | 0.97 | **1.00** | 0.94 | 0.92 | 0.93 |
| **GS** | 0.92 | 0.94 | **1.00** | 0.97 | 0.90 |
| **PCA** | 0.91 | 0.92 | 0.97 | **1.00** | 0.88 |
| **HCS** | 0.93 | 0.93 | 0.90 | 0.88 | **1.00** |

TABLE VII
CORRELATION MATRIX BETWEEN ORIGINAL, FULL-RADIOMETRICALLY CORRECTED, AND PAN-SHARPENED -BASED FCD IMAGES (AFTER RESCALING)

| | FCD Image based on the Input Data | | | | |
|---|---|---|---|---|---|
| | **Original** | **Rad_Corr** | **GS** | **PCA** | **HCS** |
| **Original** | **1.00** | 0.99 | 0.95 | 0.93 | 0.93 |
| **Rad_Corr** | 0.99 | **1.00** | 0.94 | 0.93 | 0.92 |
| **GS** | 0.95 | 0.94 | **1.00** | 0.97 | 0.89 |
| **PCA** | 0.93 | 0.93 | 0.97 | **1.00** | 0.89 |
| **HCS** | 0.93 | 0.92 | 0.89 | 0.89 | **1.00** |

In general, there were several obvious miscategorized pixels in the resultant FCD maps, both in original bands at 30 m and pan-sharpened bands at 15 m pixel sizes. For example, the herbaceous aquatic weed (*Eichhornia crassipes*) in the surrounding Rawa Pening Lake has been classified as "heterogeneous very dense forest" and "extremely dense forest". Suppose this misclassified result was caused by a vegetation index approach like NDVI (normalized difference vegetation index). In that case, it could be fully understood since NDVI is a simple transformation and is frequently reported as having a problem with saturation in very dense vegetation [11], [45]–[47]. Surprisingly, FCD transformation, which could be considered a complex approach is comprising several stages using various indices -and purposively developed to overcome the aforementioned shortcoming- could not achieve a better result.

*4) Accuracy assessment:* Accuracy assessment was carried out by referring the resultant FCD maps to independent field observation. For the FCD images containing 0-100 range pixel values, validation samples were taken using stratified random sampling. Each sample was measured based on high-spatial-resolution imagery such as WorldView-3 and Google Earth images, supported by field observation. In this case, accuracy calculation was based on the ratio data. For the FCD maps containing vegetation density classes, the validation samples were formalized into a set of polygons containing FCD categories. Since the FCD maps contained vegetation structural composition classes in combination with canopy density, the accuracy assessment was undertaken using categorical data. Fig. 8 shows the result.

The polygons were digitized using reference images at the same resolution (30 m for the original dataset and 15 m for the pan-sharpened ones), based on the measurement using high-spatial-resolution imagery and field observation. The polygons were then converted to raster format to be superimposed with each of the FCD maps. An example of a confusion matrix resulting from this process is presented in Table VIII so that each overall accuracy, user's and producer's accuracy could be derived, accompanied by the Kappa index of agreement. All overall accuracies were then compared to each other using a bar graph shown in Fig. 5.

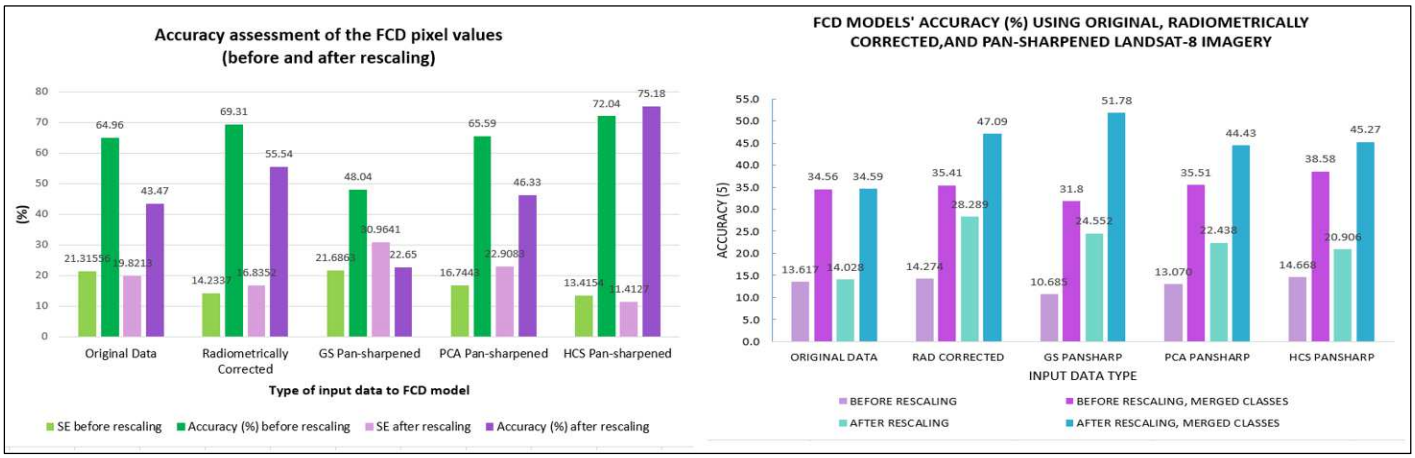


Fig. 5 LEFT: Standard errors and accuracies obtained from different datasets for two different treatments (before and after rescaling). RIGHT: Accuracy comparison between FCD maps which were generated using different datasets and different treatments

Fig. 5 also showed that the radiometrically corrected bands using full atmospheric correction method provided the best FCD map as compared to other datasets, either the original data without correction or pan-sharpened bands. Moreover, among the pan-sharpening methods, the Gram-Schmidt method could produce the most accurate FCD map. It should also be noted that the correlation coefficients between datasets did not guarantee the generated mapping accuracy. Pixel value rescaling process in each step of FCD modelling and in each dataset played more important role in this case. As shown in Fig. 5, the GS-pan-sharpening methods derived the second-highest overall accuracy, just after the radiometrically

corrected original dataset. The same problems occurred in all FCD maps, which could not provide accurate and good separation between classes.

TABLE VIII
AN EXAMPLE OF CONFUSION MATRIX SHOWING THE ACCURACY ASSESSMENT RESULT IN %, BASED ON FCD MAP GENERATED USING GRAM-SCHMIDT (GS) PAN-SHARPENED DATASET. THE UNIT OF OBSERVATION IS IN PIXEL. SEE THE FCD MAPS FOR THE CLASS CODES.

| | | Field reference FCD classes (pixels) | | | | | | | | | | | |
|---|---|---|---|---|---|---|---|---|---|---|---|---|---|
| | | **1** | **2** | **3** | **4** | **5** | **6** | **7** | **8** | **9** | **10** | **11** | **Total** |
| **FCD mapping result (pixels)** | **1** | 1004 | 819 | 36 | 9 | 0 | 6 | 0 | 0 | 0 | 0 | 0 | 1874 |
| | **2** | 1237 | 1004 | 428 | 302 | 52 | 0 | 0 | 0 | 0 | 0 | 0 | 3023 |
| | **3** | 121 | 207 | 489 | 120 | 85 | 4 | 0 | 0 | 0 | 0 | 0 | 1026 |
| | **4** | 57 | 127 | 311 | 359 | 265 | 4 | 0 | 4 | 0 | 0 | 0 | 1127 |
| | **5** | 13 | 39 | 505 | 418 | 626 | 0 | 2 | 16 | 0 | 0 | 0 | 1619 |
| | **6** | 14 | 8 | 129 | 154 | 332 | 10 | 107 | 202 | 0 | 7 | 0 | 963 |
| | **7** | 13 | 4 | 16 | 10 | 20 | 89 | 98 | 566 | 4 | 72 | 29 | 921 |
| | **8** | 5 | 0 | 2 | 0 | 0 | 413 | 153 | 185 | 56 | 379 | 212 | 1405 |
| | **9** | 2 | 0 | 0 | 0 | 0 | 1223 | 501 | 150 | 539 | 1236 | 508 | 4159 |
| | **10** | 2 | 0 | 0 | 8 | 0 | 692 | 689 | 481 | 1093 | 1022 | 136 | 4123 |
| | **11** | 0 | 0 | 0 | 2100 | 0 | 355 | 146 | 8 | 112 | 748 | 643 | 4112 |
| **Total** | | 2468 | 2208 | 1916 | 3480 | 1380 | 2796 | 1696 | 1612 | 1804 | 3464 | 1528 | **24352** |

Overall accuracy= 24.55%, Overall Kappa = 0.1699

Table VIII shows that confusion between classes 1 up to 5 was very high. The same problem existed between classes 6 up to 11. This means that the FCD model based on Gram-Schmidt pan-sharpening method did not generate a good separation between vegetation cover density and structural composition since it only reached 24.55% overall accuracy.

Furthermore, Table IX and Fig. 6 shows that the rescaling process could derive FCD maps with higher accuracy. The effect of rescaling on the accuracy increase is more significant in radiometrically corrected datasets and all pan-sharpened images. Based on the obtained results, a class merging or regrouping process was applied.

The class merging tried to consider the separation between non-vegetated/least vegetated cover, bushland and woodland, and denser multi-story forest. Therefore, classes 1 and 2 were merged, then classes 3, 4, and 5 were grouped together, classes 6 and 7 followed, remaining classes 8 up to 11 as the last group. As a result, the new accuracies for FCD map based on radiometrically corrected bands and the one based on GS pan-sharpened dataset increased to 47.09% and 51.78%.

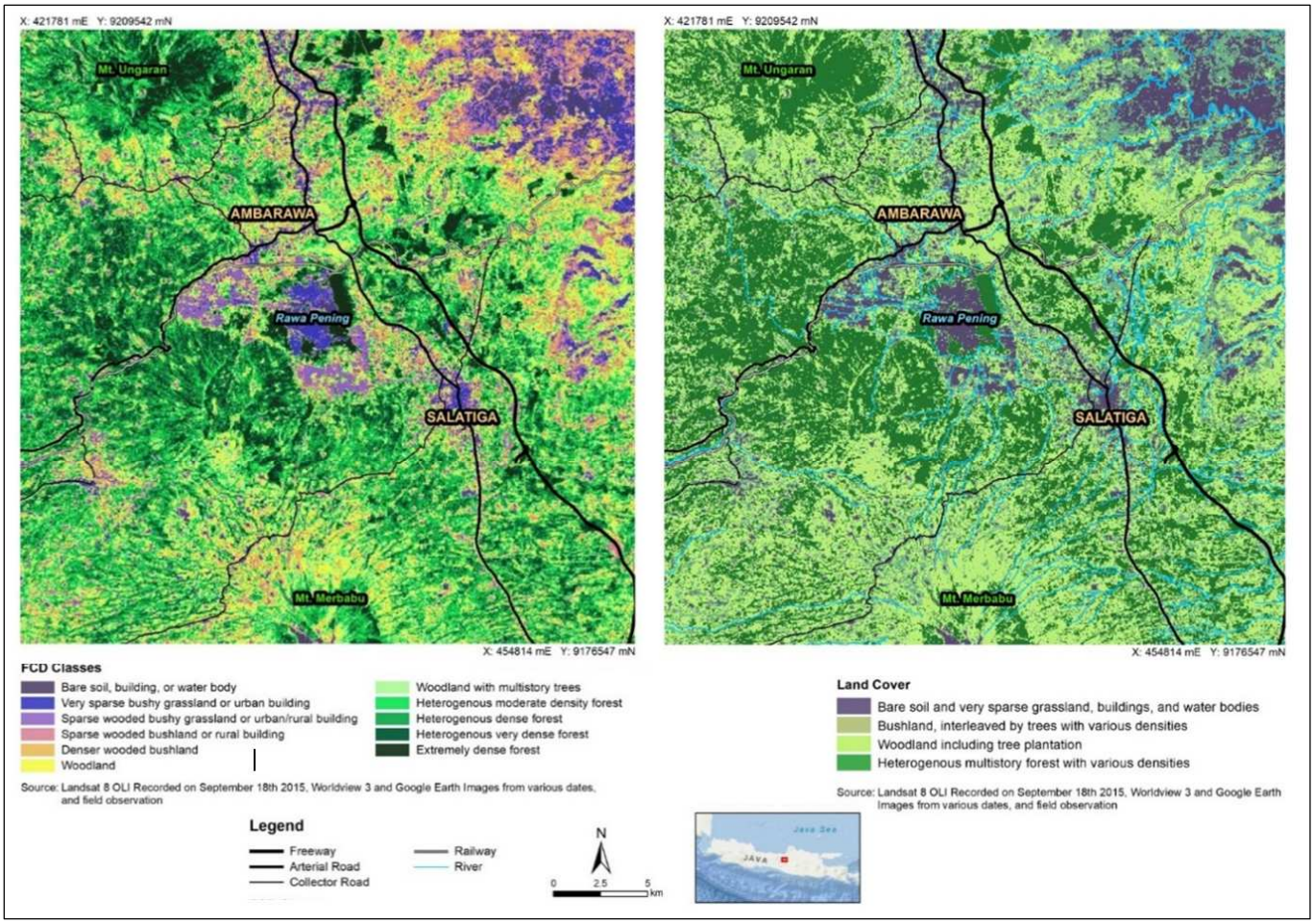


Fig. 6 LEFT: Forest cover density (FCD) map of Salatiga Ambarawa, generated from Gram-Schmidt pan-sharpened dataset of Landsat-8 OLI.. RIGHT: Land-cover map of Salatiga and Ambarawa, generated from reclassification (class merging) of original GS pan-sharpened FCD.

TABLE IX
AN EXAMPLE OF CONFUSION MATRIX SHOWING THE ACCURACY ASSESSMENT RESULT IN %, BASED ON CLASS MERGING OF FCD MAP GENERATED USING HCS PAN-SHARPENED DATASET.

| | | 1-2 | 3-5 | 6-7 | 8-11 | Total |
|---|---|---|---|---|---|---|
| Merged classes | 3-5 | 2562 | 170 | 12 | 0 | 2744 |
| | 3-5 | 1958 | 2056 | 4 | 0 | 4717 |
| | 6-7 | 136 | 1733 | 106 | 22 | 1997 |
| | 8-11 | 21 | 2117 | 4370 | 7886 | 14894 |
| | **Total** | **4676** | **6776** | **4492** | **8408** | **24352** |

**Overall accuracy** = 51.78%, Kappa = 0.3094

1-2 Bare soil and very sparse grassland, buildings, water bodies
3-5 Bushland interleaved by trees at various densities
6-7 Woodland (including tree plantation)
8-11 Heterogeneous multi-story forest with various densities

This study found that the FCD method failed to map the spatial distribution of vegetation cover density and structural composition in a complex landscape like Salatiga and Ambarawa areas. The landform varies, the land-use types are very heterogeneous, and the range of elevation is very large. A swampy lake with aquatic weed of *Eichhornia crassipes* caused very low values in brightness index (BI) image, which contributed to the misidentification of extremely dense forest during the derivation of vegetation density (VD) image. High elevation areas caused low thermal index (TI) image values, which might contribute to the misidentification of higher density vegetation cover when the data was integrated with the shadow index (SI). In general, all woodland classes (classes 1 and 2) were misidentified. The same problem came up with classes 6 and 7, which were mostly misidentified. High-density rubber plantation was also misclassified as very dense heterogeneous forest.

On the other hand, the use of pan-sharpening methods changed the pixel values of the original bands, and finally, they lowered the accuracy of derived models, *i.e.*, FCD maps. Studies carried out by Danoedoro *et al.* [26] also found that pan-sharpening methods produced datasets that were inaccurately classified compared to the original multispectral bands. It is also important to note that with 15 m spatial resolution, the identification of heterogeneous forest was difficult because the pixel size might contain only one or two large tree canopies. That is to say. The 15 m spatial resolution could be too high for such a mapping purpose. A further study needs to be carried out in the future concerning this issue.

Based on the obtained results, an example of the best FCD map using GS pan-sharpened dataset after rescaling is given in Fig 6-left, which has an overall accuracy of 24.55%. Another version of the FCD map generated from the GS pan-sharpening method has been regrouped into fewer classes, which achieved 51.78%. Overall accuracy is shown in Fig 6-right.

## IV. CONCLUSION

This study concluded that atmospheric correction was strongly required in FCD modeling. However, the Landsat-8 data with 16-bit coding experienced a problem when it was processed using standard FCD transformation. A rescaling process of the results was required to be undertaken, although this is contrary to the initial concept of FCD development, which should not need such a process. The pan-sharpening process altered the original pixel values that had been radiometrically corrected and thus changed the quality of the derived spectral-based FCD models. Consequently, all FCD maps generated from pan-sharpened datasets showed relatively low accuracies, so that further processing in terms of class merging or regrouping was required. However, the achieved overall accuracies were not still satisfactory. Therefore, the applicability of FCD transformation needs to be tested in various landscape characteristics with different modern satellite image datasets.

## ACKNOWLEDGMENT

The authors are grateful to Dr. Prima Widayani, Dr. Iswari Nur Hidayati, and Dr.Sc. Sanjiwana Arjasakusuma for reviewing the manuscript prior to the submission.

## REFERENCES

[1] J. G. Zaehringer Llopis, J.C., Latthachack, P. Tun Tun Thein, T.T., and Heinimann, A, "A novel participatory and remote-sensing-based approach to mapping annual land use change on forest frontiers in Laos, Myanmar, and Madagascar," *J. Land Use Sci.*, vol. 13, no. 1–2, pp. 16–31, 2018, doi: 10.1080/1747423X.2018.1447033.

[2] J. Deka, O.P. Tripathi, and M. L. Khan, "Implementation of Forest Canopy Density Model to Monitor Tropical Deforestation," *J. Indian Soc. Remote Sens.*, vol. 41, no. 2, pp. 469–475, 2013.

[3] P. Danoedoro, "Multidimensional Land-use Information for Local Planning and Land Resources Assessment in Indonesia: Classification Scheme for Information Extraction from High-Spatial Resolution Imagery," *Indones. J. Geogr.*, vol. 51, no. 2, pp. 131–146, 2019, doi: 10.22146/ijg.32781.

[4] Y. Xi *et al.*, "Mapping Tree Species Composition Using OHS-1 Hyperspectral Data and Deep Learning Algorithms in Changbai Mountains, Northeast China," *Forests*, vol. 10, no. 818, pp. 2–17, 2019, doi: 10.3390/f10090818.

[5] P. Danoedoro *et al.*, "Developing interpretation methods for detailed categorization-based land-cover/land-use mapping at 1:50,000 scale in Indonesia," in *Sixth International Symposium on LAPAN-IPB Satellite,* 2019, vol. 11372.

[6] M. Y. McPartland *et al.*, "Characterizing Boreal Peatland Plant Composition and Species Diversity with Hyperspectral Remote Sensing," *Remote Sens.*, vol. 11, pp. 1685–1716, 2019, doi: 10.3390/rs11141685.

[7] K. C. Hennessy and M. Lewis, "Hyperspectral Classification of Plants: A Review of Waveband Selection Generalisability," *Remote Sens.*, vol. 12, no. 113, pp. 2–27, 2019, doi: 10.3390/rs12010113.

[8] W. Zhao, T. Mu, and D. Li, "Classification of hyperspectral images based on two-channel convolutional neural network combined with support vector machine algorithm," *J. Applied. Remote Sensing,* vol. 14, no. 2, pp. 2–17, 2020.

[9] P. Danoedoro, "Multisource Classification for Land-Use Mapping Based on Spectral, Textural, and Terrain Information Using Landsat Thematic Mapper Imagery A Case Study of Semarang-Ungaran Area," *Indones. J. Geogr.*, vol. 35, no. 2, pp. 81–106, 2003.

[10] E. F. Berra and R. Gaulton, "Remote sensing of temperate and boreal forest phenology: A review of progress, challenges and opportunities in the intercomparison of in-situ and satellite phenological metrics," *For. Ecol. Manage.*, vol. 480, pp. 1–17, 2020, doi: 10.106/j.foreco.2020.118663.

[11] J. Xue and B. Su, "Significant Remote Sensing Vegetation Indices: A Review of Developments and Applications," *J. Sensors*, vol. 2017, pp. 1–17, 2017, doi: 10.1155/2017/1353691.

[12] R.P. Dewa and P. Danoedoro, "The effect of image radiometric correction on the accuracy of vegetation canopy density estimate using several Landsat-8 OLI's vegetation indices: A case study of Wonosari area," in *the 4th LISAT Conference*, 2017, vol. 54, no. 1, doi: 10.1088/1755-1315/54/1/012046.

[13] A. Rikimaru, P.S. Roy, and S. Miyatake, "Tropical forest cover density mapping," *Trop. Ecol.*, vol. 43, no. 1, pp. 39–47, 2002.

[14] H. van Gils, I. S. Zonneveld, W. van Wijngaarden, A. Kannegieter, and H. Huizing, *Land Ecology and Land-use Survey*. Enschede: International Institute for Aerospace Survey and Earth Sciences (ITC), 1990.

[15] S. Pladsrichua, R. Suwanwerakamtorn, and N. Pannucharoenwong, "Estimating Vegetation Canopy Density in the Lower Chi Basin, Northeast,Thailand Using Landsat Data," *Int. J. Appl. Eng. Res.*, vol. 13, no. 6, pp. 3215–3219, 2018.

[16] B. Bera, S. Saha, and S. Bhattacharjee, "Estimation of Forest Canopy Cover and Forest Fragmentation Mapping Using Landsat Satellite Data of Silabati River Basin (India)," *KN - J. Cartogr. Geogr. Inf.*, vol. 70, no. 4, pp. 181–197, 2020, doi: 10.1007/s42489-020-00060-1.

[17] A. Abdollahnejad, D. Panagiotidis, and P. Surovy, " Forest canopy density assessment using different approaches – Review," *J. For. Sci.*, vol. 63, no. 3, pp. 106–115, 2020, doi: 10.17221/110/2016-JFS.

[18] S. Himayah, Hartono, and P. Danoedoro, "Pemanfaatan Citra Landsat 8 Multitemporal dan Model Forest Canopy Density (FCD) untuk Analisis Perubahan Kerapatan Kanopi Hutan di Kawasan Fakultas Geografi Universitas Gadjah Mada Gunung Kelud, Jawa Timur," *Maj. Geogr. Indones.*, vol. 51, no. 1, pp. 65–72, 2017, doi: 10.22146/mgi.24236.

[19] M. Ismail, Hartono., and P. Danoedoro, "The Application of Forest Cover Density (FCD) Model for Structural Composition of Vegetation Changes in Part of Lore Lindu National Park, Central Sulawesi Province," in *5th Geoinformation Science Symposium*, 2017, vol. 98, no. 012056.

[20] R. Ahmed, "Temporal Assessment of Forest Canopy Density Around Hojai-Diphu Railway Line in Assam, India," *Int. J. Sci. Technol. Res.*, vol. 9, no. 03, pp. 3040–3043, 2020.

[21] J. G. Liu and J. Mason, *Image Processing and GIS for Remote Sensing: Techniques and Applications,*. London: Wiley-Blackwell, 2016.

[22] H. Sunuprapto, P. Danoedoro, and S. Ritohardoyo, "Evaluation of pan-sharpening method: applied to artisanal gold mining monitoring in Gunung Pani Forest area," in *2nd International Symposium on LAPAN-IPB Satellite for Food Security and Environmental Monitoring, LISAT-FSEM*, 2016, vol. 33, pp. 230–238.

[23] J. R. Eastman, *TerrSet Geospatial Monitoring and Modeling System - Manual*. Morcester, MA: Clark Labs, 2020.

[24] Q. K. Rahaman, Q. . Hassan, and M. . Ahmed, "Pan-Sharpening of Landsat-8 Images and Its Application in Calculating Vegetation Greenness and Canopy Water Contents," *ISPRS Int. J. Geo-Information*, vol. 6, no. 168, pp. 1–16, 2019, doi: 10.3390/ijgi6060168.

[25] X. Meng, H. Shen, H. Li, L. Zhang, and R. Fu, "Review of the pansharpening methods for remote sensing images based on the idea of meta-analysis: Practical discussion and challenges," *Inf. Fusion*, vol. 46, pp. 102–113, 2019, doi: 10.1016/j.inffus.2018.05.006.

[26] P. Danoedoro, T. Ardiansyah, and Adiwijoyo, "Perbandingan Hasil Klasifikasi Per-Piksel dan Klasifikasi Berbasis Objek menggunakan Citra ALOS Pan-Sharpened: Studi Kasus Daerah Pinggiran Kota Yogyakarta," 2018.

[27] P. Danoedoro and A. Zukhrufiyati, "Integrating Spectral Indices and Geostatistics based on Landsat-8 Imagery for Surface Clay Content Mapping in Gunung Kidul Area, Yogyakarta, Indonesia," 2015.

[28] P. S. Chavez, "Image-Based Atmospheric Corrections Revisited and Improved," *Photogramm. Eng. Remote Sens.*, vol. 62, no. 9, pp. 1025–1036, 1996.

[29] E. G. Jones, S. Wong, A. Milton, J. Sclauzero, H. Whittenbury, and M. D. and McDonnell, "The Impact of Pan-Sharpening and Spectral Resolution on Vineyard Segmentation through Machine Learning," *Remote Sens.*, vol. 12, no. 6, pp. 1–24, 2020, doi: 10.3390/rs12060934.

[30] A. Rasul, H. Balzter, G. R. F. Ibrahim, H. M. Hameed, J. Wheeler, and P. M. Najmaddin, "Applying Built-Up and Bare-Soil Indices from Landsat 8 to Cities in Dry Climates," *Land*, vol. 7, no. 81, pp. 1–13, 2018, doi: 10.3390/land7030081.

[31] Y. Xu, L. Wang, K. W. Ross, C. Liu, and K. Berry, "Standardized Soil Moisture Index for Drought Monitoring Based on Soil Moisture Active Passive Observations and 36 Years of North American Land Data Assimilation System Data: A Case Study in the Southeast United States," *Remote Sens.*, vol. 10, no. 301, pp. 1–13, 2018, doi: 10.3390/rs10020301.

[32] Y. Wang *et al.*, "Mapping tropical disturbed forests using multi-decadal 30 m optical satellite imagery," *Remote Sens. Environ.*, vol. 221, pp. 474–488, 2019, doi: 10.1016/j.rse.2018.11.028.

[33] V. Vani, K.P. Kumar, and M. V Ravibabu, "Temperature and vegetation indices-based surface soil moisture estimation: a remote sensing data approach," in *International Conference on Remote Sensing for Disaster Management*, 2019, pp. 281–289.

[34] ITTO/JOFCA, *FCD-Mapper Ver.2 User Guide, Semi-Expert Remote Sensing System for Canopy Density Mapping*. ITTO/JOFCA, 2003.

[35] I.N. Ananda, A. F. Umela, N. Ratnasari, D. A. Putri, Y. S. Wulandari, and P. Danoedoro, "Development of land-cover spatial database using satellite imagery: lesson learned from southern part of Sumatera," in *Sixth Geoinformation Science Symposium*, 2019, vol. 11311, doi: 10.1117/12.2548890.

[36] J. Deka, O. P. Tripathi, M. L. Khan, and V. K. Srivastava, "Study on land-use and land-cover change dynamics in Eastern Arunachal Pradesh, N.E. India using remote sensing and GIS," *Trop. Ecol.*, vol. 60, pp. 199–208, 2019, doi: 10.1007/s42965-019-00022-3.

[37] S. Godinho *et al.*, "Assessment of environment, land management, and spatial variables on recent changes in Montado land cover in southern Portugal," *Agroforest Syst.*, no. 90, pp. 177–192, 2016, doi: 10.1007/s10457-014-9757-7.

[38] C. Li, M. Li, and Y. Li, "Improving estimation of forest aboveground biomass using Landsat 8 imagery by incorporating forest crown density as a dummy variable," *Can. J. For. Res.*, vol. 50, no. 4, pp. 390–398, 2020, doi: 10.1139/cjfr-2019-0216.

[39] R. M. Sukarna, "Aplikasi Model Forest Canopy Density Citra Landsat 7 ETM untuk Menentukan Indeks Luas Tajuk (Crown Area Index) Dan Kerapatan Tegakan (Stand Density) Hutan Rawa Gambut Di DAS Sebangau Provinsi Kalimantan Tengah," *Maj. Geogr. Indones.*, vol. 22, no. 1, pp. 1–21, 2008.

[40] C. Li, Y. Li, and M. Li, "Improving forest aboveground biomass (AGB) estimation by incorporating crown density and using Landsat 8 OLI images of a subtropical forest in Western Hunan in Central China," *Forests*, vol. 10, no. 104, pp. 1–14, 2019.

[41] A. P. P. Hartoyo, L. B. Prasetyo, I. Z. Siregar, Supriyanto, I. Theilade, and U. J. Siregar, "Carbon Stock Assessment Using Forest Canopy Density Mapper In Agroforestry Land In Berau, East Kalimantan, Indonesia," *Biodiversitas*, vol. 20, no. 9, pp. 2661–2676, 2019, doi: 10.13057/biodiv/d200931.

[42] S. Dittmann, E. Thiessen, and E. and Hartung, "Applicability of Different Non-invansive Methods for Tree Mass Estimation: A Review," *For. Ecol. Manage.*, no. 398, pp. 2018–2215, 2017, doi: 10.1016/j.foreco.2017.05.013.

[43] N.Y. Krakauer, T. Lakhankar, and J. D. Anadón, "Mapping and Attributing Normalized Difference Vegetation Index Trends for Nepal," *Remote Sens.*, vol. 9, no. 986, pp. 1–15, 2017, doi: 10.3390/rs9100986.

[44] T. Dawson, J.S.O. Sandoval, V. Sagan, and and T. Crawford, "A Spatial Analysis of the Relationship between Vegetation and Poverty," *Int. J. Geo-information*, vol. 7, no. 83, pp. 1–26, 2018, doi: 10.3390/ijgi7030083.

[45] A.A. Tesfaye and B. G. Awoke, "Evaluation of the saturation property of vegetation indices derived from sentinel-2 in mixed crop-forest ecosystem," *Spat. Inf. Res.*, vol. 29, no. 1, pp. 109–121, 2021, doi: 10.1007/s41324-020-00339-5.

[46] F. Carneiro M, C. E. A. Furlani, C. Zerbato, P. C. de Menezes, L. A. da Silva Gírio, and M. F. de Oliveira, "Comparison between vegetation indices for detecting spatial and temporal variabilities in soybean crop using canopy sensors," *Precis. Agric.*, 2019.

[47] Q. Ma, Y. Su, L. Luo, L. Li, M. Kelly, and Q. Guo, "Evaluating the uncertainty of Landsat-derived vegetation indices in quantifying forest fuel treatments using bi-temporal LiDAR data," *Ecol. Indic.*, vol. 95, pp. 298–310, 2018, doi: 10.1016/j.ecolind.2018.07.050.